

Revealing room temperature ferromagnetism in exfoliated Fe₅GeTe₂ flakes with quantum magnetic imaging

Hang Chen^{1*}, Shahidul Asif^{2*}, Matthew Whalen^{1*}, Jeyson Támara-Isaza^{1,3}, Brennan Luetke¹, Yang Wang¹, Xinhao Wang¹, Millicent Ayako¹, Andrew F. May⁴, Michael A. McGuire⁴, Chitrleema Chakraborty^{1,2}, John Q. Xiao^{1,†}, and Mark J.H. Ku^{1,2,†}

¹*Department of Physics and Astronomy, University of Delaware, Newark, Delaware 19716, United States*

²*Department of Materials Science and Engineering, University of Delaware, Newark, Delaware 19716, United States*

³*Departamento de Física, Universidad Nacional de Colombia, Bogotá D.C., Colombia*

⁴*Materials Science and Technology Division, Oak Ridge National Laboratory, Oak Ridge, Tennessee 37831, United States*

* These authors contributed equally to this work.

† Corresponding authors: mku@udel.edu, jqx@udel.edu

Abstract

Van der Waals material Fe₅GeTe₂, with its long-range ferromagnetic ordering near room temperature, has significant potential to become an enabling platform for implementing novel spintronic and quantum devices. To pave the way for applications, it is crucial to determine the magnetic properties when the thickness of Fe₅GeTe₂ reaches the few-layers regime. However, this is highly challenging due to the need for a characterization technique that is local, highly sensitive, artifact-free, and operational with minimal fabrication. Prior studies have indicated that Curie temperature T_C can reach up to close to room temperature for exfoliated Fe₅GeTe₂ flakes, as measured via electrical transport; there is a need to validate these results with a measurement that reveals magnetism more directly. In this work, we investigate the magnetic properties of exfoliated thin flakes of van der Waals magnet Fe₅GeTe₂ via a quantum magnetic imaging technique based on nitrogen vacancy diamond. Through imaging the stray fields, we confirm room-temperature magnetic order in Fe₅GeTe₂ thin flakes with thickness down to 7 units cell. The stray field patterns and their response to magnetizing fields with different polarities point to a perpendicular easy-axis anisotropy. Furthermore, we perform imaging at different temperatures and determine the Curie temperature of the flakes at ≈ 300 K. These results provide the basis for realizing a room-temperature monolayer ferromagnet with Fe₅GeTe₂. This work also demonstrates that the imaging technique enables a rapid screening of multiple flakes simultaneously, thereby paving the way towards high throughput characterization of potential 2D magnets near room temperature.

Keywords: Fe₅GeTe₂, 2D magnet, quantum sensing.

Quasi-two-dimensional (2D) van der Waals (vdW) crystals with long-range ferromagnetic (FM) order have attracted enormous attention in the past few years for their potential applications in the development of next-generation devices¹⁻⁴. Their 2D nature enables high degree of tunability by electrostatic field, pressure, and strain. As they do not require lattice matching, a wide range of heterostructure can be

fabricated with other materials to utilize interfacial phenomena or to create new phases of matter. Compared to traditional magnetic materials with 3D structures, their highly tunable nature and readiness for drastic miniaturization presents 2D magnets as promising platforms for implementing a variety of important applications, including new magnetic memory, spintronics devices, and hybrid quantum systems based on magnons. However, the low Curie temperatures (T_C) common to these materials impede their applications at room temperature; for example, both CrGeTe_3 and CrI_3 have $T_C \approx 60 \text{ K}$ ^{5, 6}, while Fe_3GeTe_2 has $T_C \approx 230 \text{ K}$ ^{7, 8} and 130 K ¹ for bulk crystal and monolayer, respectively. Recently, Fe_5GeTe_2 has been identified as a cleavable material holding intrinsic magnetic order near the room temperature in both bulk and thin flake limit^{2, 9-12}, which nominates it as a suitable candidate for 2D-based devices. In addition, the magnetization has been shown to be tunable by cobalt and nickel substitution, with T_C increasing upon doping and antiferromagnetic behavior is even observed^{7, 13, 14}. So far, magnetization of Fe_5GeTe_2 bulk crystal has been characterized via magnetometry, which does not have sufficient sensitivity for exfoliated flakes that are more relevant for devices. For thin flakes, electrical transport measurement has provided indication of near-room temperature T_C ^{9, 12, 15}. However, it is a global measurement which conceals the local magnetic information, and probes magnetism indirectly. A local, sensitive detector of magnetic field generated by magnetization will provide the direct validation of room temperature magnetism in exfoliated thin flakes of Fe_5GeTe_2 .

In this work, we employ quantum magnetic imaging (QMI) technique based on nitrogen vacancy (NV) centers in diamond to observe room-temperature magnetism in exfoliated Fe_5GeTe_2 thin flakes down to 21 nm (7 units cell) and investigate their magnetic properties, including T_C and anisotropy. The NV center in diamond realizes a powerful quantum sensor of magnetic field due to its high-sensitivity and high spatial resolution^{16, 17}. Therefore, NV magnetometry provides an enabling tool for studying novel phenomena in condensed matters and material science. The use of NV centers as magnetic field probe can be implemented as scanning probe microscopy with single NVs¹⁸⁻²⁰ or optical wide field imaging with NV ensembles^{21, 22}. The former allows an ultra-high spatial resolution, with $\sim\text{nm}$ resolution possible, but due to the need for pixel-by-pixel scanning, is limited in its field of view, is time-consuming to measure multiple samples, and is often limited to point-measurement in a sweep (e.g., field or temperature sweep) which may miss crucial information in the evolution of the samples. Wide-field imaging has resolution limited by optical diffraction (resolution 570 nm in our system), but is capable of parallel acquisition of multiples samples, and hence is suitable for rapid characterization, and can access the evolution of samples across a large area during a sweep. Furthermore, optical wide field imaging is significantly simpler to implement compared to NV scanning probe microscopy.

QMI in this work is realized via a bulk diamond crystal with NV ensembles, and the magnetic stray field is measured with continuous-wave optically detected magnetic resonance (cw-ODMR)²³. Mapping the stray field of the sample allows the analysis of local magnetic properties in sub-micron scale. We first confirm our QMI is capable of detecting stray fields and that such stray fields originate from room-temperature ferromagnetism in exfoliated Fe_5GeTe_2 flakes, which are protected with a thin Pt layer to prevent degradation. Then, we conduct both thickness-dependent and temperature-dependent measurements on the flakes; the results reveal the magnetic phase transition and provide insights on anisotropy in Fe_5GeTe_2 flakes. Lastly, we demonstrate the utility of our QMI system in characterizing multiple exfoliated flakes in a wide-field view and demonstrate that unprotected flakes exhibit room-temperature magnetism with thickness down to at least 45 nm.

RESULTS AND DISCUSSION

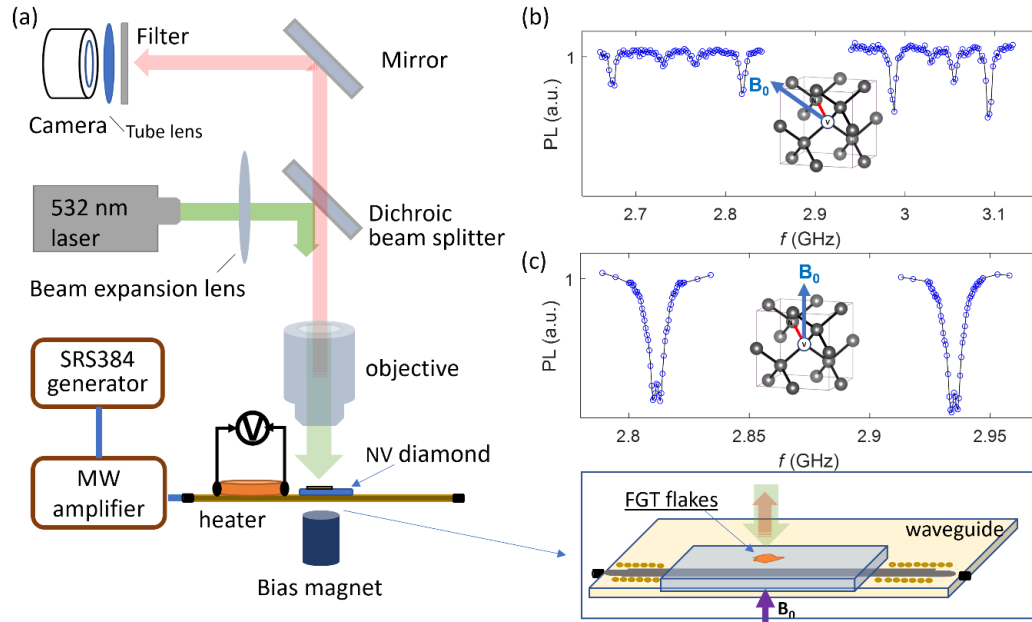


Fig. 1. (a) Schematic of the widefield NV QMI. The green laser is directed on Fe_5GeTe_2 flakes sitting on top of a diamond with NV ensembles near the surface. The PL emitted by NVs (red arrow line) is separated from the excitation via the dichroic beam splitter, further filtered via an interference filter, and imaged onto a camera. The NV diamond is attached on a signal line which delivers microwave for the ODMR measurement. The magnetic bias field is generated by a permanent magnet placed underneath the printed circuit board (PCB). An electrical heater is placed on the PCB near to the flake sample, allowing the temperature dependent measurement on the flakes (b) The bias field is tuned along a direction where one obtains an ODMR spectrum including all 4 pairs of NV spin transitions. (c) The ODMR spectrum measured when the bias field is applied in the z direction.

The schematic of QMI is described in Fig. 1a. NV centers are optically excited with a 532-nm laser which illuminates an area $\sim 40 \mu\text{m}$ in size, and the NV photoluminescence (PL) is imaged onto a camera. The diamond with exfoliated Fe_5GeTe_2 flakes sits on the signal line of a co-planar waveguide where the microwave is delivered into. A permanent magnet, movable via translational stages, supplies a bias field for splitting the ODMR resonances. In principle, there can be up to four pairs of ODMR resonances, each corresponding to $m_s = 0 \leftrightarrow \pm 1$ transitions of NVs aligned with one of the four diamond crystalline axes; the direction of the nitrogen-vacancy bond provides the quantization axis for the corresponding NV. We employ two configurations of bias field B_0 . First, bias field can be applied at such a direction as to split all four ODMR resonances (Fig. 1b). In this configuration, we sense B_{NV} , projection of the magnetic field along an NV quantization axis of our choice; B_{NV} has contribution from both the out-of-plane and in-plane field. In a second configuration, we align B_0 along the z direction (normal to diamond surface), which allows us to sense B_z , the projection of field along the z direction. More details can be found in **Methods** section. Fig. 1b and c show example ODMR spectra for two configurations of bias field B_0 . The extraction of B_{NV} and B_z from ODMR spectra has been demonstrated in **S1** in the Supporting Information.

All measurements are performed in atmosphere. Mapping stray fields from the ODMR measurements is described in S2 in the Supporting Information.

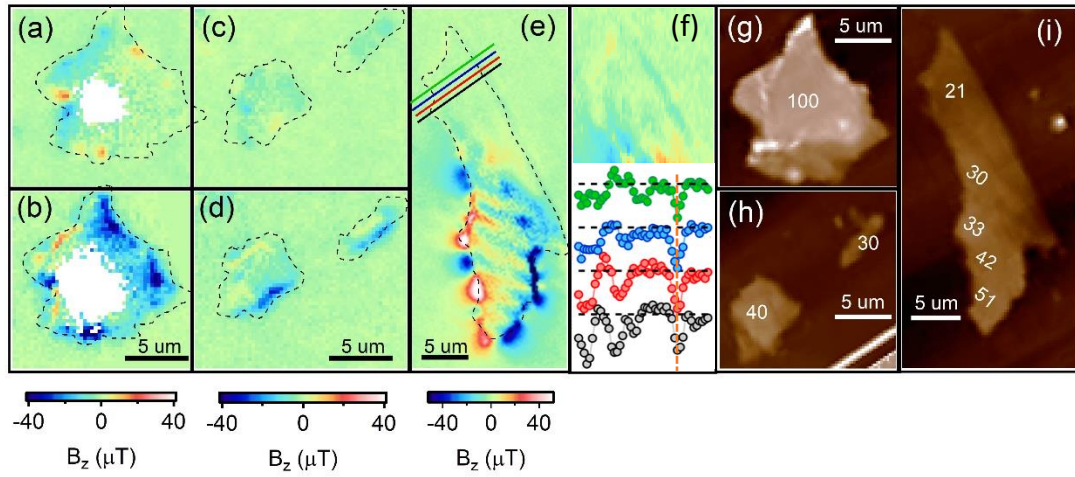


Fig. 2. Ferromagnetism in exfoliated thin flakes of Fe_5GeTe_2 . The NV stray field B_z mappings of the thickest Fe_5GeTe_2 flake (center thickness ~ 100 nm) magnetically initialized by pole 1 in (a) and pole 2 in (b) of a permanent magnet. Flake with thickness of 40 nm (left) and 30 nm (right) magnetized by pole 1 in (c) and pole 2 in (d). These measurements are performed under the B_z configuration. It is noted that data on the pixels with low SNR (e.g., when the error of ΔB_z larger than $300 \mu\text{T}$) has been removed in image plotting. (e) B_z stray field mapping of the thinnest flake with thickness of 21 nm. In all images, we display ΔB_z , which is the change of B_z from background. (f) Top: zoomed-in view of the upper part of the flake shown in (e), displayed over a range of -20 to $+20 \mu\text{T}$. Bottom: Stray field variation along the four linecuts marked in (e). Each curve has a vertical offset for clarity of display. Horizontal black dashed lines indicate zero ΔB_z value for each of the curves. Curves are correlated to the linecuts in (e) by different colors. In each curve, the left peak and right dip clearly indicate the boundary of the thinnest part. In particular, a sharp dip manifests along the right boundary, which is marked with vertical orange dashed line. (g)-(i) AFM images of the 4 measured flakes where the thicknesses of flakes are labeled by the numbers in the unit of nanometers. The outlines of the flakes in panel (a) to (e) have been depicted with black dash lines.

We first confirm that NV magnetometer is able to detect the stray field signal from the flakes in ambient condition - at room temperature and in atmosphere, and that the stray field has its origin from ferromagnetism in the flakes. Prior to imaging, Fe_5GeTe_2 flakes protected with Pt layer are magnetized by one side (pole 1) of a cylindrical permanent magnet *ex situ* with magnetic field about 0.6 T. We then conduct ODMR measurement with a bias field $B_0 = 40$ G in z direction. A bias field is necessary in order to split the lower and upper ODMR transitions and hence identify the sign of the stray field; the bias field is always applied in the direction of pole 2. The analyzed stray fields of a 100 nm thick flake magnetized by pole 1 is plotted in Fig. 2a. Subsequently, we magnetize the flakes again but with the opposite pole (pole 2) of the permanent magnet. We then perform measurement in a similar bias field $B_0 = 30$ G. The field mapping result is shown in Fig. 2b. We note that measurements occurred at two different bias fields because the diamond position slightly changes with respect to the permanent magnet underneath the

printed circuit board (PCB) when each time the diamond is mounted after the magnetizing procedure. Nevertheless, the signal contribution from the bias field has been removed in all colormaps in Fig. 2 by subtracting the signal from the area without the flakes, and hence we are able to display ΔB_z , the change of stray field from the background. A small and slowly-varying background may remain in ΔB_z due to inhomogeneity of the bias field from the permanent magnet.

A single domain magnet with homogeneous out-of-plane magnetization produces a ΔB_z pattern that has strong amplitude at the flake boundary, while in the inner parts of the flake the stray field is weaker but still significant (see **S3** in the Supporting Information). If the magnetization is in-plane, ΔB_z instead is localized at a pair of opposite edges, and is vanishingly small in the inner part of the flake. More generally, the flakes may have domains or may have magnetic textures, which will produce more complex ΔB_z pattern, hence the experimentally imaged stray field will not necessarily have all the matching features compared to that of an idealized single domain magnet. Nevertheless, in general, one anticipates stray field signal along the boundary and more generally across the flake, if magnetization is present. Indeed, in Fig. 2a-e, significant stray field is observed that is associated with the flake. The question then is whether the stray field comes from paramagnetism or ferromagnetically ordered magnetization. If the flakes are paramagnetic, we would expect a stray field that is not affected by the magnetization procedure, and in fact should be slightly weaker in Fig. 2b (with bias field 30G) compared to in Fig. 2a (bias field 40G). Instead, we observe the contrary, where Fig. 2b shows a generally much stronger stray field amplitude compared to Fig. 2a. Clearly, the measured stray fields show significant difference in strength when we magnetize the flake in opposite directions. This result is consistent with the presence of ferromagnetically ordered magnetization: when the magnetization is polarized along the opposite directions, one polarization will show a stronger magnetization (and hence stray field) in the same or even a smaller bias field. We note that this analysis does not require the flake to have a single magnetic domain, as we have access to local stray field. Our result indicates that the detected signal indeed comes from the magnetization change in the flake. Similar observations are found in other two smaller flakes with thickness of 40 nm and 30 nm as shown in Fig. 2c and d. Therefore, we conclude the stray field observed is generated by ferromagnetism in the flakes.

The topology of the stray field provides insights in the magnetic anisotropy of the flakes. In Fig. 2b, we observe stray field of mostly the same sign (namely negative) along the edge as well as in the inner part of the flake; additional features in the stray field are likely due to domain or magnetic textures. This topology appears to match with the expected stray field distribution induced by a perpendicular magnetization²⁴; on the other hand, an in-plane magnetization would have led to ΔB_z pattern localized to the boundary and is vanishingly small in the inner part of the flake, where in our experiment, stray field that is readily observable is generally present well into the interior of the flake. We note that the center of the thicker flakes has low signal-to-noise ratio (SNR). This is because the thick flakes attenuate light and reduces the number of collected photons. When the thickness of the exfoliated flake decreases to 40 nm (left flake in Fig. 2c and d), we are able to obtain higher SNR around the flake center. In Fig. 2d, we once again note that stray field is generally present across the entire flake. Lastly, we note the contrast between Fig. 2a and b (as well as between Fig. 2c and d) indicates the change on magnetization induced by a perpendicular magnetizing field persists after the magnetizing field has been removed. Aspects of these results point to easy-axis anisotropy near T_C , though further investigation is required to draw certain conclusions. For instance, the stray field appears to remain across a flake, though the existence of domains could lead to apparent sign inversions within a given flake that may also give the appearance of in-plane anisotropy. Future measurements at higher and variable bias fields would provide even more

insight into the magnetism in these and similar materials in this thin flake form, and in particular allow more definitive conclusions about anisotropy.

Lastly, we explore what is the thinnest flake we have observed that exhibits room temperature ferromagnetism. We display the stray field map of a 21 nm thick flake in Fig. 2e. Fig. 2f shows a zoomed-in view of the upper part of the flake, which is the thinnest part of this flake; it clearly displays stray field near the boundary (stray fields along four linecuts in Fig. 2e are displayed in Fig. 2f), which demonstrates the ability of our wide-field NV magnetometer to characterize the stray field induced by very thin flake. Hence, we demonstrate Fe_5GeTe_2 , when protected with a thin Pt layer, exhibits ferromagnetism in flakes as thin as 21 nm, corresponding to 7 unit cells. The thicknesses of all those flakes are measured by the atomic force microscopy (AFM) as shown in Fig. 2g, h and i. We note that in Fig. 2i multiple terraces are present in the bottom half of the flake, as revealed by AFM, and may be responsible for the complex stray field pattern in the bottom half of Fig. 2e.

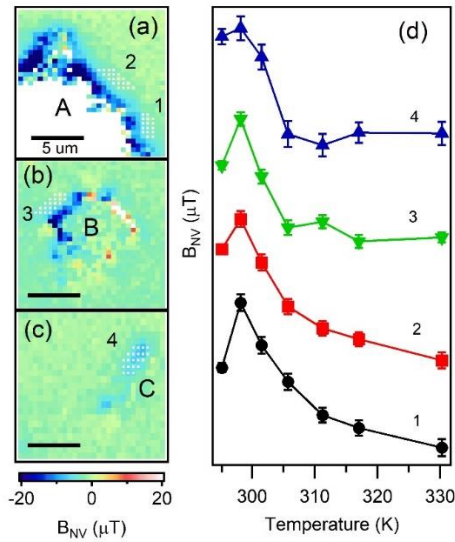


Fig. 3. (a)-(c) NV stray field images B_{NV} of Fe_5GeTe_2 flakes A, B and C at room temperature. The numbers label the areas where we investigate the temperature dependence of stray field. The pixel points of these areas are marked by the white dots. (d) The temperature dependence of stray field averaged from the selected area. Each curve is offset in the y-axis for clarity. The black circles, red squares, green down-pointing triangles and blue up-pointing triangles indicate the averaged stray fields of area 1, 2, 3 and 4, respectively.

Having confirmed that the flakes are ferromagnetic at room temperature, a natural question to ask is what are the Curie temperatures of the flakes. To answer this question, we take advantage of the ability to perform simultaneous magnetometry and thermometry with NVs to map the stray field at different temperatures. In this measurement, an electrical heater is placed on the PCB near the diamond chip to enable temperature tuning above the room temperature. Here, we employ the configuration in Fig. 1b to measure B_{NV} , which is more convenient for simultaneous magnetometry and thermometry. The details of temperature calibration are in S3 in the Supporting Information.

We first heat up the sample to 330 K which is higher than the widely reported Curie temperature T_C of Fe_5GeTe_2 material^{2, 9, 12}, and then perform magnetic imaging measurements as we continuously decrease the temperature down to room temperature. This allows us to form a magnetic phase diagram of the magnetization by examining the magnetization-induced stray field, from which the T_C can be determined. At several temperatures, we perform ODMR measurement to obtain magnetic images. The same ODMR measurement allows us to extract the temperature (see **S4** in the Supplementary Information). In this work, temperature fluctuation is less than 1 K within a measurement cycle at each temperature point. We examine the temperature dependence of B_{NV} of the 3 flakes in Fig. 2g and 2h. In Fig. 3a, we show the stray field mapping measured at room temperature and mark the areas where we focus on the investigation of temperature dependence. For the thicker flakes A (the same flake as in Fig. 2a and b) and B (the flake on the left of Fig. 2c and d), we necessarily have to focus on the stray field closer to the edges due to the lower SNR in the center, as noted before, where for the thinner flake C we are able to look at the stray field right at the flake. We note that here we measure ΔB_{NV} , which has contribution from both out-of-plane and in-plane stray field, and hence has different topology compared to the measurement in Fig. 2. This configuration is employed here as it is more convenient for temperature-dependent measurement (see **S5** in the Supplementary Information), and we are only concerned with how the local stray field evolves with temperature.

The average stray field of the selected regions are plotted as a function of temperature in Fig. 3b. With increasing the temperature, all B_{NV} vs. T curves show an initial increase or no change from room temperature (295 K) to ~ 300 K, and then quickly decrease to a constant value. We attribute the divergence-like behavior of the curves near ~ 300 K to the phase transition from ferromagnetic (FM) to paramagnetic (PM) order in Fe_5GeTe_2 flakes. The observed initial upturn in each curve has also been observed in M vs T measurement of CrI_3 , an easy-axis van der Waals magnet, when the bias is in-plane, and is attributed to the softening of anisotropy near T_C ²⁵. This scenario is consistent with our evidence for out-of-plane anisotropy and the fact that B_0 has a significant in-plane component in this measurement. The T_C is determined from the location where the B_{NV} vs. T curve begins a rapid descent, and we find $T_C \approx 300$ K for all selected regions. We do not observe any particular thickness dependence of T_C from Fig. 3c, which is consistent with the observation in Ref⁹.

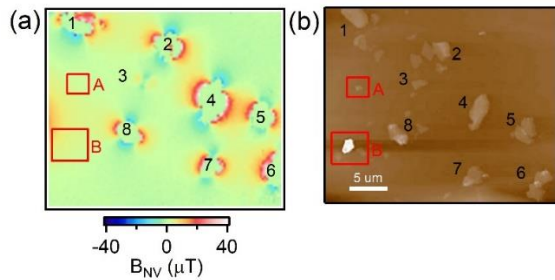


Fig. 4. (a) The B_{NV} stray field map of Fe_5GeTe_2 flakes without Pt protection layer. Stray field in areas where SNR is low is not shown. (b) The AFM image of the flakes in (a). The flake or the flakes cluster are labeled by numbers and the measured flakes thicknesses are #1(45~80 nm), #2(35~100 nm), #3(40~65 nm), #4(110 nm), #5(75~150 nm), #6(85 nm), #7(60 nm), #8(100 nm).

At last, we demonstrate the utility of our QMI technique for rapid screening of magnetism in exfoliated flakes. Multiple Fe_5GeTe_2 flakes without Pt protection layer are imaged at room temperature and the stray field map is shown in Fig. 4a. We note that in this measurement, B_{NV} was imaged, hence the stray field pattern looks different from those in Fig. 2. As discussed previously, SNR of stray field measurement is low near the center of the flakes, so the stray field values are not displayed for these pixel points. The AFM image of the corresponding flakes is shown in Fig. 4b. We have properly labeled the flakes or flake clusters in both panels. It is seen that some small flakes are visible in AFM picture (for example, flakes circled by red boxes A and B) but do not generate stray field. This may be attributed to the fact that those flakes are too small or too thin and hence have completely degraded in the absence of protective layer. However, even some larger flakes (for example, the flakes around the cluster #2) also do not generate stray field, which may also indicate complete degradation. Among the flakes that generate stray fields, we find the thinnest flake is 40 nm thick (< 20 unit cells). This result shows our imaging tool can measure the magnetism of unprotected Fe_5GeTe_2 flake also down to very thin layers. It also provides an option to investigate the degradation of the magnetic flakes in an ambient condition by imaging the sample field changing with time. Lastly, this work demonstrates the utility of QMI for rapid, parallel characterization of the thin flakes of other potential 2D magnets near room temperature, providing an enabling tool that will aid the effort in discovering additional 2D magnets that are useful for applications.

CONCLUSION

In conclusion, we have employed QMI based on NV ensemble in diamond to study the magnetism of exfoliated Fe_5GeTe_2 thin flakes at room temperature. The measured stray fields have been confirmed to originate from the ferromagnetic moments in the flakes by the observation of different field intensities after magnetizing the flakes in opposite directions. The stray field patterns and response to magnetizing field point to the scenario that perpendicular easy axis anisotropy dominates in these flakes. Room-temperature ferromagnetism is observed in flake with thicknesses as low as 21 nm (7 units cell). The temperature dependent measurements allow us to determine the Curie temperature of the flakes $T_C \approx 300$ K which is higher than the room temperature and independent of the flake thickness in the range of 21 to 100 nm. These results pave the way towards realizing room-temperature monolayer ferromagnet with Fe_5GeTe_2 . As a novel tool for characterizing microscopic magnetic materials and structures, our imaging technique provides a sensitive and artifact-free way to detect the minute signal of local magnetism. At last, we demonstrate the utility of our QMI setup in rapid screening of magnetism in exfoliated flakes, which enables the parallel measurement of many flakes at room temperature and provide a useful tool for characterization and screening of other potential near-room-temperature 2D magnets.

METHODS

Sample preparation.

Electronic grade diamonds with a $\{100\}$ -front facet are commercially obtained (Element Six), created using chemical vapor deposition. Diamonds are implanted with nitrogen (Innovion). Implantation density is in the range of $\sim 10^{12}$ - 10^{13} cm^{-2} , and implantation energy is 6 keV which leads to an average NV depth ~ 20 nm²⁶. The implanted diamonds are subsequently annealed. We fabricate markers on the diamond surface with NVs via lithography and electron-beam evaporation in order to facilitate identification of flakes.

The bulk single crystals of $\text{Fe}_{5-x}\text{GeTe}_2$ were grown and characterized as discussed in Refs. ⁹ and ¹⁰. The crystals were quenched from the growth temperature and washed with ethanol and acetone. These quenched, metastable crystals were then cooled to 10K or less in a magnetometer. This cycling to cryogenic temperatures results in a first-order magnetostructural transition near 100K that increases the bulk Curie temperature from ≈ 270 to 310K. This unusual behavior is discussed in detail in Ref. ¹⁰ where such crystals are identified as type ‘Q-C’. The Fe content has not been controlled during these growths, which are done in the presence of iodine, and the average composition is expected to be near $\text{Fe}_{4.7}\text{GeTe}_2$. The Fe_5GeTe_2 crystals are initially stored in a vacuum desiccator to avoid sample degradation. We exfoliate flakes on the diamond surface with NVs. Exfoliation was performed with a standard medium tack Blue Plastic Film tape (Semiconductor Equipment Corporation P/N 18074). Exfoliation was done quickly in the air, and then the sample was immediately transferred into an electron-beam evaporation chamber for deposition of a 5 nm Pt layer as a protection layer to prevent degradation. In this work, we have investigated both flakes protected with Pt layer and flakes without protective layer.

Experimental setup

We use a 532-nm laser (Coherent Verdi 2G) in QMI system. A Kohler-illumination system, consisting of a beam expansion lens and an objective (Olympus ULWD MSPlan80 0.75 NA), expands the laser beam to illuminate an area of about $40 \times 40 \mu\text{m}^2$ on the sample. NV photoluminescence (PL) is collected by the same objective. The collected light passes through a 552-nm edge dichroic (Semrock LM01-552-25), after which it is separated from the excitation, passes through another 570-nm long-pass filter to further reduce light not in the PL wavelength range, and is imaged via a tube lens (focal length $f = 200$ mm) onto a camera (Basler acA1920-155um). Each pixel corresponds to 133 nm on the sample (265 nm if an additional 2x2 binning is applied). Estimated number of NVs that contribute to the signal of a pixel is >10 . A SRS384 signal generator supplies microwave (MW) to an amplifier to produce MW with power of 45 dBm. The microwave is delivered into the signal line of a co-planner waveguide on a printed circuit board (PCB), which produces an in-plane MW magnetic field for driving NV spin transition. In our experiment, the diamond surface with exfoliated Fe_5GeTe_2 flakes and NVs may be either facing up or down.

Measurement and analysis protocol

We perform ODMR by sweeping MW frequency f , and at each f we acquire an image, $I(x,y,f)$. To achieve sufficient signal-to-noise ratio (SNR), data acquisition on the order of hours may be required. To deal with sample drift during acquisition, we employ the following innovation in NV wide imaging. We repeatedly perform ODMR measurement to obtain a series of $I_i(x,y,f)$, each of which is saved separately. During post-processing, we align and sum images to obtain a single $I(x,y,f)$. We then fit the ODMR spectrum at each pixel, from which we extract a magnetic field map $B_\alpha(x,y)$, where α =NV or z depending on the configuration of bias field employed.

Acknowledgement: MW and JQX are supported by NSF through the University of Delaware Materials Research Science and Engineering Center DMR-2011824; additional support is received from NSF DMR grant #1904076. CC acknowledges support from the University of Delaware Research Foundation. Crystal growth and characterization (AFM, MAM) were supported by the U.S. Department

of Energy, supported by the U. S. Department of Energy, Office of Science, Basic Energy Sciences, Materials Sciences and Engineering Division.

1. Fei, Z.; Huang, B.; Malinowski, P.; Wang, W.; Song, T.; Sanchez, J.; Yao, W.; Xiao, D.; Zhu, X.; May, A. F.; Wu, W.; Cobden, D. H.; Chu, J. H.; Xu, X., Two-dimensional itinerant ferromagnetism in atomically thin Fe_3GeTe_2 . *Nat Mater* **2018**, 17 (9), 778-782.
2. Stahl, J.; Shlaen, E.; Johrendt, D., The van der Waals Ferromagnets $\text{Fe}_{5-\delta}\text{GeTe}_2$ and $\text{Fe}_{5-\delta-x}\text{Ni}_x\text{GeTe}_2$ - Crystal Structure, Stacking Faults, and Magnetic Properties. *Zeitschrift für anorganische und allgemeine Chemie* **2018**, 644 (24), 1923-1929.
3. Tan, C.; Lee, J.; Jung, S. G.; Park, T.; Albarakati, S.; Partridge, J.; Field, M. R.; McCulloch, D. G.; Wang, L.; Lee, C., Hard magnetic properties in nanoflake van der Waals Fe_3GeTe_2 . *Nat Commun* **2018**, 9 (1), 1554.
4. Joe, M.; Yang, U.; Lee, C., First-principles study of ferromagnetic metal Fe_5GeTe_2 . *Nano Materials Science* **2019**, 1 (4), 299-303.
5. Gong, C.; Li, L.; Li, Z.; Ji, H.; Stern, A.; Xia, Y.; Cao, T.; Bao, W.; Wang, C.; Wang, Y.; Qiu, Z. Q.; Cava, R. J.; Louie, S. G.; Xia, J.; Zhang, X., Discovery of intrinsic ferromagnetism in two-dimensional van der Waals crystals. *Nature* **2017**, 546 (7657), 265-269.
6. Huang, B.; Clark, G.; Navarro-Moratalla, E.; Klein, D. R.; Cheng, R.; Seyler, K. L.; Zhong, D.; Schmidgall, E.; McGuire, M. A.; Cobden, D. H.; Yao, W.; Xiao, D.; Jarillo-Herrero, P.; Xu, X., Layer-dependent ferromagnetism in a van der Waals crystal down to the monolayer limit. *Nature* **2017**, 546 (7657), 270-273.
7. May, A. F.; Calder, S.; Cantoni, C.; Cao, H.; McGuire, M. A., Magnetic structure and phase stability of the van der Waals bonded ferromagnet $\text{Fe}_{3-x}\text{GeTe}_2$. *Physical Review B* **2016**, 93 (1).
8. Liu, S.; Yuan, X.; Zou, Y.; Sheng, Y.; Huang, C.; Zhang, E.; Ling, J.; Liu, Y.; Wang, W.; Zhang, C.; Zou, J.; Wang, K.; Xiu, F., Wafer-scale two-dimensional ferromagnetic Fe_3GeTe_2 thin films grown by molecular beam epitaxy. *npj 2D Materials and Applications* **2017**, 1 (1).
9. May, A. F.; Ovchinnikov, D.; Zheng, Q.; Hermann, R.; Calder, S.; Huang, B.; Fei, Z.; Liu, Y.; Xu, X.; McGuire, M. A., Ferromagnetism Near Room Temperature in the Cleavable van der Waals Crystal Fe_5GeTe_2 . *ACS Nano* **2019**, 13 (4), 4436-4442.
10. May, A. F.; Bridges, C. A.; McGuire, M. A., Physical properties and thermal stability of $\text{Fe}_{5-x}\text{GeTe}_2$ single crystals. *Physical Review Materials* **2019**, 3 (10).
11. Li, Z.; Xia, W.; Su, H.; Yu, Z.; Fu, Y.; Chen, L.; Wang, X.; Yu, N.; Zou, Z.; Guo, Y., Magnetic critical behavior of the van der Waals Fe_5GeTe_2 crystal with near room temperature ferromagnetism. *Sci Rep* **2020**, 10 (1), 15345.
12. Ohta, T.; Sakai, K.; Taniguchi, H.; Driesen, B.; Okada, Y.; Kobayashi, K.; Niimi, Y., Enhancement of coercive field in atomically-thin quenched Fe_5GeTe_2 . *Applied Physics Express* **2020**, 13 (4).
13. May, A. F.; Du, M.-H.; Cooper, V. R.; McGuire, M. A., Tuning magnetic order in the van der Waals metal Fe_5GeTe_2 by cobalt substitution. *Physical Review Materials* **2020**, 4 (7).
14. Tian, C.; Pan, F.; Xu, S.; Ai, K.; Xia, T.; Cheng, P., Tunable magnetic properties in van der Waals crystals $(\text{Fe}_{1-x}\text{Co}_x)_5\text{GeTe}_2$. *Applied Physics Letters* **2020**, 116 (20).
15. Ohta, T.; Tokuda, M.; Iwakiri, S.; Sakai, K.; Driesen, B.; Okada, Y.; Kobayashi, K.; Niimi, Y., Butterfly-shaped magnetoresistance in van der Waals ferromagnet Fe_5GeTe_2 . *AIP Advances* **2021**, 11 (2).
16. Casola, F.; van der Sar, T.; Yacoby, A., Probing condensed matter physics with magnetometry based on nitrogen-vacancy centres in diamond. *Nature Reviews Materials* **2018**, 3 (1).
17. Ku, M. J. H.; Zhou, T. X.; Li, Q.; Shin, Y. J.; Shi, J. K.; Burch, C.; Anderson, L. E.; Pierce, A. T.; Xie, Y.; Hamo, A.; Vool, U.; Zhang, H.; Casola, F.; Taniguchi, T.; Watanabe, K.; Fogler, M. M.; Kim, P.; Yacoby, A.; Walsworth, R. L., Imaging viscous flow of the Dirac fluid in graphene. *Nature* **2020**, 583 (7817), 537-541.

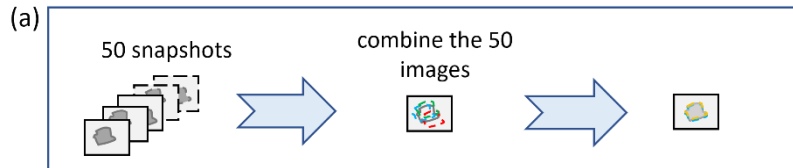
18. Maletinsky, P.; Hong, S.; Grinolds, M. S.; Hausmann, B.; Lukin, M. D.; Walsworth, R. L.; Loncar, M.; Yacoby, A., A robust scanning diamond sensor for nanoscale imaging with single nitrogen-vacancy centres. *Nat Nanotechnol* **2012**, 7 (5), 320-4.
19. Fabre, F.; Finco, A.; Purbawati, A.; Hadj-Azzem, A.; Rougemaille, N.; Coraux, J.; Philip, I.; Jacques, V., Characterization of room-temperature in-plane magnetization in thin flakes of CrTe₂ with a single-spin magnetometer. *Physical Review Materials* **2021**, 5 (3).
20. Sun, Q. C.; Song, T.; Anderson, E.; Brunner, A.; Forster, J.; Shalomayeva, T.; Taniguchi, T.; Watanabe, K.; Grafe, J.; Stohr, R.; Xu, X.; Wrachtrup, J., Magnetic domains and domain wall pinning in atomically thin CrBr₃ revealed by nanoscale imaging. *Nat Commun* **2021**, 12 (1), 1989.
21. Pham, L. M.; Le Sage, D.; Stanwix, P. L.; Yeung, T. K.; Glenn, D.; Trifonov, A.; Cappellaro, P.; Hemmer, P. R.; Lukin, M. D.; Park, H.; Yacoby, A.; Walsworth, R. L., Magnetic field imaging with nitrogen-vacancy ensembles. *New Journal of Physics* **2011**, 13 (4).
22. Broadway, D. A.; Scholten, S. C.; Tan, C.; Dontschuk, N.; Lillie, S. E.; Johnson, B. C.; Zheng, G.; Wang, Z.; Oganov, A. R.; Tian, S.; Li, C.; Lei, H.; Wang, L.; Hollenberg, L. C. L.; Tetienne, J. P., Imaging Domain Reversal in an Ultrathin Van der Waals Ferromagnet. *Adv Mater* **2020**, 32 (39), e2003314.
23. Barry, J. F.; Turner, M. J.; Schloss, J. M.; Glenn, D. R.; Song, Y.; Lukin, M. D.; Park, H.; Walsworth, R. L., Optical magnetic detection of single-neuron action potentials using quantum defects in diamond. *Proceedings of the National Academy of Sciences* **2016**, 113 (49), 14133-14138.
24. Tetienne, J. P.; Broadway, D. A.; Lillie, S. E.; Dontschuk, N.; Teraji, T.; Hall, L. T.; Stacey, A.; Simpson, D. A.; Hollenberg, L. C. L., Proximity-Induced Artefacts in Magnetic Imaging with Nitrogen-Vacancy Ensembles in Diamond. *Sensors (Basel)* **2018**, 18 (4).
25. Liu, Y.; Wu, L.; Tong, X.; Li, J.; Tao, J.; Zhu, Y.; Petrovic, C., Thickness-dependent magnetic order in CrI₃ single crystals. *Sci Rep* **2019**, 9 (1), 13599.
26. Tetienne, J. P.; de Gille, R. W.; Broadway, D. A.; Teraji, T.; Lillie, S. E.; McCoey, J. M.; Dontschuk, N.; Hall, L. T.; Stacey, A.; Simpson, D. A.; Hollenberg, L. C. L., Spin properties of dense near-surface ensembles of nitrogen-vacancy centers in diamond. *Physical Review B* **2018**, 97 (8).

Supplementary Information

S1. Stray field calculation from B_{NV} and B_z configuration.

(1) The axis set by the nitrogen and vacancy provides the quantization axis of an NV, and it may point along one of the four possible crystallographic directions. The projection of the total magnetic field (the sum of sample stray field and an applied bias field) on each axis, B_{NV} , contributes to the shift of ODMR resonance [1]. Off-axis field also contributes to the shift of ODMR resonance; however, the leading order off-axis contribution is common-mode motion between the upper and the lower transitions, and in our analysis procedure, we only look at the differential shift, hence we are not sensitive to off-axis field. When the bias field is fixed, the shifts in ODMR resonance reveals the amplitude of the sample field projected along the crystallographic direction. In general, an ODMR spectrum includes four pairs of transitions due to the Zeeman splitting as shown in Fig. 1b. (2) While if B_0 is applied in z direction (normal to diamond surface), only one pair of transitions is observed as shown in Fig. 1c because the field projection on each crystallographic direction is equal. As a matter of fact, applying B_0 in z direction results in an enhanced contrast in the ODMR spectrum since it is the sum of contribution from all four NV axis, as long as the bias is not large ($B \lesssim 100$ G) and hence the effect of off-axis field on photoluminescence contrast is not strong. The enhanced contrast in this configuration is confirmed by the comparison of resonance contrast between Fig. 1b and Fig. 1c where 4 transitions on each side are overlapped. However, it might also broaden the linewidth due to the frequency shift of resonances induced by even a slight misalignment between B_0 and z direction. The broaden linewidth as a result reduces the sensing sensitivity. Therefore, good alignment is crucial in B_z configuration. The frequency splitting between lower and upper resonance transitions can be written by $\Delta f = 2\gamma_{NV}(B_{0,NV} + B_{NV})$ where $\gamma_{NV} = 28.03$ GHz/T is the NV gyromagnetic ratio, $B_{0,NV}$ and B_{NV} are the bias field and sample stray field projected on the corresponding NV axis [2]. Thus, the stray field is calculated by $B_{NV} = (\Delta f / 2\gamma_{NV}) - B_{0,NV}$. While in B_z configuration, the stray field B_z is calculated by the formula $B_z = \sqrt{3}(\Delta f / 2\gamma_{NV}) - B_0$ according to the geometric relationship between bias field and NV axis [3].

S2. ODMR spectra fitting and stray field mapping.



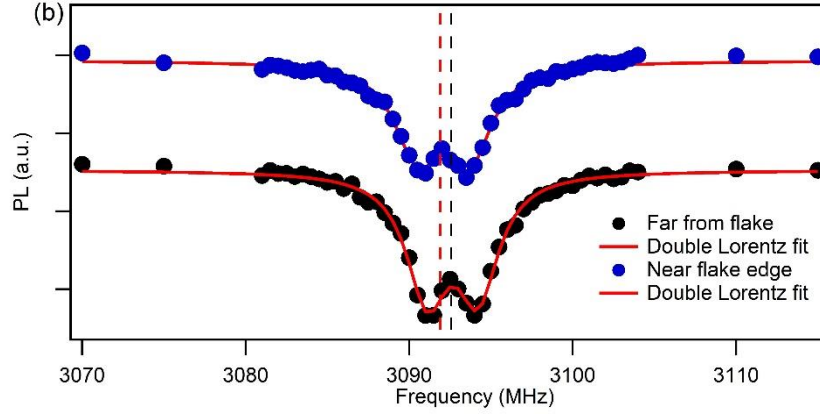


Fig. S2. (a) Diagram of the data analysis. In a single ODMR imaging measurement, we sweep MW frequency f and capture an image at each f . We repeat this ODMR imaging measurement for the flakes of interest more than 50 times. The collected images are properly aligned and summed to improve signal-to-noise, and then subsequently analyzed for ODMR spectrums fitting. (b) Fit to ODMR spectrums measured near the flake edge and far from the flake. Red dashed line indicates the resonance position of the former spectrum, while black dashed line indicates the resonance position of the latter spectrum.

By sweeping the MW frequency, the camera records an ODMR spectrum for each pixel. Thus, mapping of the sample field is realized by extracting resonances from each pixel. We scan the microwave frequency between 2.65~2.70 GHz and 3.07~3.11 GHz to obtain the branch of the two transitions with the largest frequency span. We repeat PL imaging of the sample N times ($N > 50$) and the recorded images are added up to reduce the noise in measured ODMR spectrums. However, misalignment might occur among recorded images due to the drift of sample position in x - y plane. As described in Fig. S2, the displaced images could be corrected via aligning the contours of the imaged flakes. This is a necessary step before we sum up the images. The summed image will be followed with pixel binning to further improve the signal to noise ratio (SNR) in the image. We analyze each pixel in the binned image by fitting the ODMR spectrum with a double-Lorentz function. The lineshape is a result of hyperfine splitting due to ^{15}N nuclear spins. The fitted values of resonance frequency are used to calculate the stray field at the corresponding pixel, which allows us to map the entire imaged region. It is noted that in the final mapping result we discard the contribution from the external magnetic field B_0 by subtracting the average of the image region without flakes.

In Fig2S (b), we show the two ODMR spectrums which are measured from a pixel near to the flake-A edge and one pixel far away from the flake. Here, we only show the resonance of upper transition ($m_s=0 \leftrightarrow +1$). The resonant peaks are fitted using a double-Lorentz formula and the center of the peak is used to determine Δf . It is observed that the ODMR peak position shifts to a lower frequency in the presence of a magnetic material, which indicates the generated negative stray field from flake-A.

S3. Stray field simulation under B_z configuration.

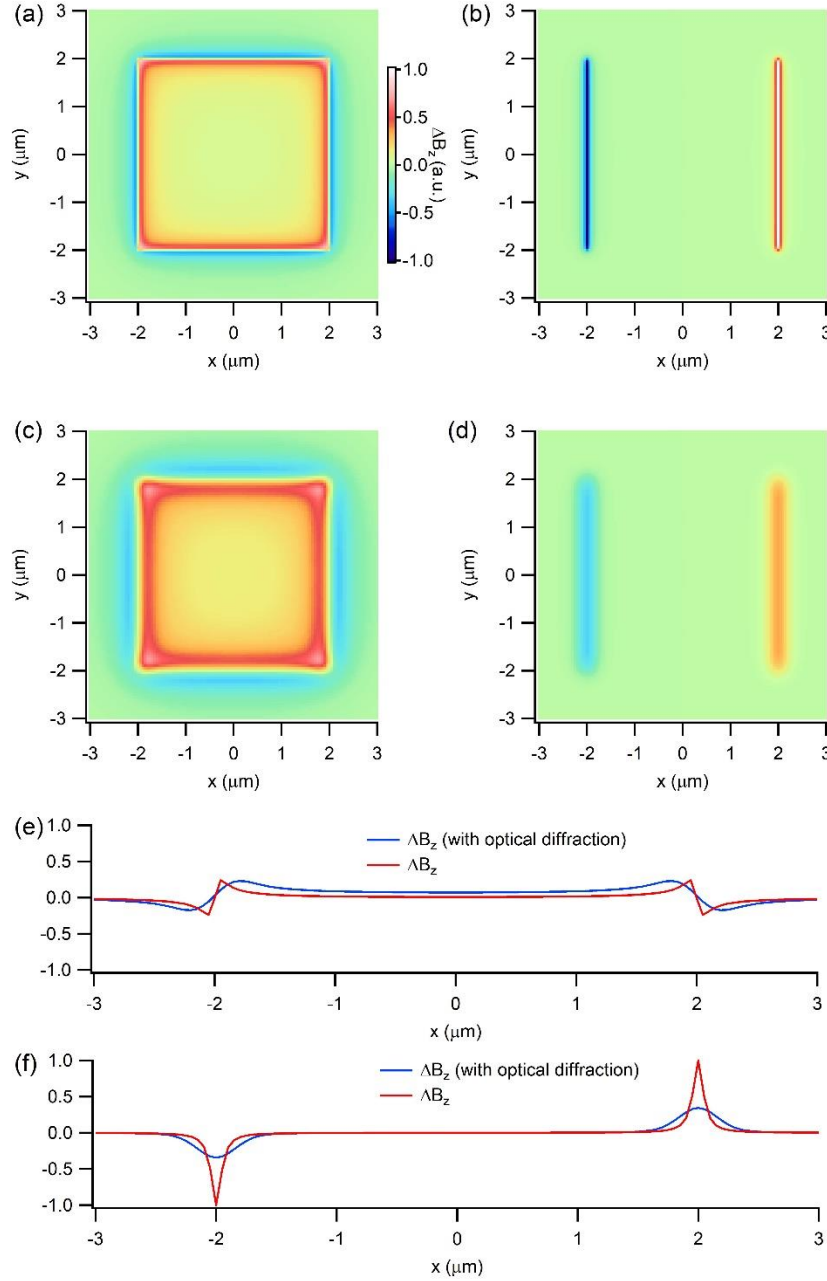


Fig. S3. Simulation of stray fields ΔB_z generated by a $2 \mu\text{m} \times 2 \mu\text{m}$ magnet with out-of-plane magnetization (a) and in-plane magnetization (pointing along x -direction) (b). (c) and (d) display the stray field patterns when the optical diffraction has been taken into account. (e) ΔB_z from the linecuts at $y=0$ in (a) and (c). (f) ΔB_z from the linecuts at $y=0$ in (b) and (d).

We numerically simulate the stray fields generated from a small square magnet. The stray field mapping of the magnet with out-of-plane magnetization in Fig. S3 (a) and (c) shows a centrosymmetric pattern. In addition, the largest intensity contrast is observed around the edge of the magnet. For magnet magnetized in-plane (along x direction), stray field shows largest intensity at the two edges with the opposite signs as

shown in in Fig. S3 (b) and (d). The sign change of the stray fields also has been displayed in the linecuts across the $y=0$ as shown in in Fig. S3 (e) and (f).

S4. Calibration of sample temperature.

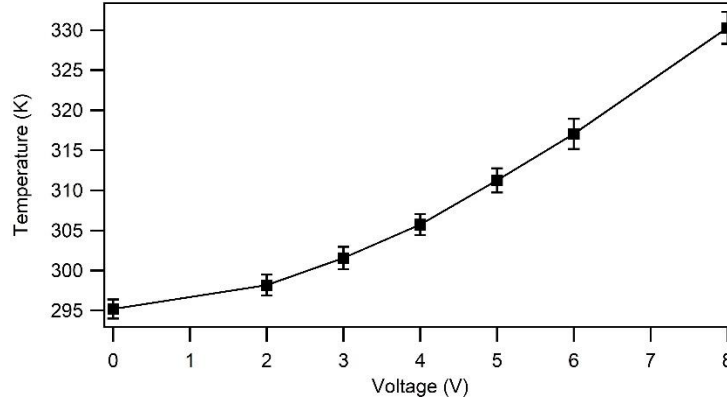


Fig. S4. Sample temperature as a function of the voltage applied for the heater.

The temperature can be calibrated from the zero-field splitting (ZFS) D . The dependence of the D on temperature is given by $dD/dT = -74$ kHz/K [4], which can be used to estimate the sample temperature. calculated by $T_0 - \Delta f_{\text{CM}} \cdot (dT/dD)$, where T_0 is the room temperature and $\Delta f_{\text{CM}} = (f_1 + f_2)/2$ is the mean of the upper and the lower transition (f_2 and f_1 respectively).

When heater is applied to change the temperature, the temperature of the bias magnet may change as it is not too far from the heater, while the sample itself may move around. Both of these can lead to the bias field at the sample changes somewhat in both the magnitude and direction. Therefore, measurement of ΔB_z would require re-alignment of the magnet at each temperature point; otherwise, ODMR lines are not overlapped sufficiently, which increase the linewidth and decrease measurement sensitivity. If all the ODMR resonances are split (as in B_{NV} configuration), then there is no need for such re-alignment at each temperature. Since we are only interested in the evolution of local stray field vs the temperature, we apply the B_{NV} configuration for our temperature dependent measurements and the sample temperature has been calibrated as shown in Fig. S3.

S5. Comparison of B_z and B_{NV} configurations in temperature dependent measurement.

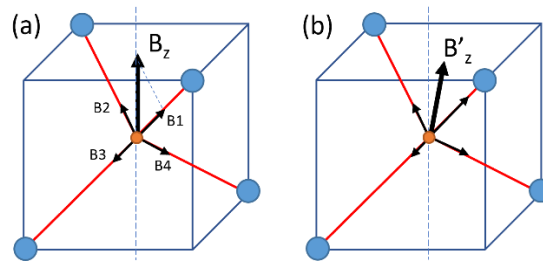


Fig. S5. (a) Projection of magnetic field on 4 NV axes under the measurement of B_z configuration. (b)

In B_z configuration, the components of B_z that projected on four NV axes are equal, i.e., $B_1=B_2=B_3=B_4$ as shown in Fig. S5(a). Therefore, the measured four ODMR spectra overlap that one only observes one resonant peak with high contrast. However, this B_z configuration is not convenient for temperature dependent measurement. Heating of the system also varies the temperature of the magnet somewhat and hence modifies the bias field in amplitude or direction as shown in Fig. S5(b). The four components are no longer equal. Thus, the four resonant peaks might not aligned once the temperature has changed, and the offset of the spectra result in a broader peak especially when the measured field is small, which will decrease the sensitivity of our measurement. On the other side, we do not have this concern under B_{NV} configuration because four resonant peaks are split and temperature induced offset on peak position does not affect our measurement sensitivity.

- [1] J. F. Barry, J. M. Schloss, E. Bauch, M. J. Turner, C. A. Hart, L. M. Pham, and R. L. Walsworth, "*Sensitivity optimization for NV-diamond magnetometry*", *Reviews of Modern Physics* **92** (2020).
- [2] E. V. Levine, M. J. Turner, P. Kehayias, C. A. Hart, N. Langellier, R. Trubko, D. R. Glenn, R. R. Fu, and R. L. Walsworth, "*Principles and techniques of the quantum diamond microscope*", *Nanophotonics* **8**, 1945 (2019).
- [3] M. J. H. Ku *et al.*, "*Imaging viscous flow of the Dirac fluid in graphene*", *Nature* **583**, 537 (2020).
- [4] R. Schirhagl, K. Chang, M. Loretz, and C. L. Degen, "*Nitrogen-vacancy centers in diamond: nanoscale sensors for physics and biology*", *Annu Rev Phys Chem* **65**, 83 (2014).